Spin Hall Effect and Origins of Nonlocal Resistance in Adatom-Decorated Graphene

D. Van Tuan,[1,2] J. M. Marmolejo-Tejada,[3,4] X. Waintal,[5] B. K. Nikolić,[3,*] S. O. Valenzuela,[1,6] and S. Roche[1,6,†]
[1]Catalan Institute of Nanoscience and Nanotechnology (ICN2), CSIC and The Barcelona Institute of Science and Technology, Campus UAB, Bellaterra, 08193 Barcelona, Spain
[2]Department of Electrical and Computer Engineering, University of Rochester, Rochester, New York 14627, USA
[3]Department of Physics and Astronomy, University of Delaware, Newark, Delaware 19716-2570, USA
[4]School of Electrical and Electronics Engineering, Universidad del Valle, Cali AA 25360, Colombia
[5]Univ. Grenoble Alpes, INAC-PHELIQS, F-38000 Grenoble, France and CEA, INAC-PHELIQS, F-38000 Grenoble, France
[6]ICREA—Institució Catalana de Recerca i Estudis Avançats, 08010 Barcelona, Spain
(Received 19 February 2016; published 20 October 2016)

Recent experiments reporting an unexpectedly large spin Hall effect (SHE) in graphene decorated with adatoms have raised a fierce controversy. We apply numerically exact Kubo and Landauer-Büttiker formulas to realistic models of gold-decorated disordered graphene (including adatom clustering) to obtain the spin Hall conductivity and spin Hall angle, as well as the nonlocal resistance as a quantity accessible to experiments. Large spin Hall angles of ∼0.1 are obtained at zero temperature, but their dependence on adatom clustering differs from the predictions of semiclassical transport theories. Furthermore, we find multiple background contributions to the nonlocal resistance, some of which are unrelated to the SHE or any other spin-dependent origin, as well as a strong suppression of the SHE at room temperature. This motivates us to design a multiterminal graphene geometry which suppresses these background contributions and could, therefore, quantify the upper limit for spin-current generation in two-dimensional materials.

DOI: 10.1103/PhysRevLett.117.176602

Over the past decade, the spin Hall effect (SHE) has evolved rapidly from an obscure theoretical prediction to a major resource for spintronics [1,2]. In the direct SHE, the injection of a conventional unpolarized charge current into a material with extrinsic (due to impurities) or intrinsic (due to band structure) spin-orbit coupling (SOC) generates a pure spin current in the direction transverse to the charge current. Although the SHE was first observed only a decade ago [3], it is already ubiquitous within spintronics as the standard pure spin-current generator and detector [1,2]. The spin Hall angle θ_{sH}, as the ratio of generated spin Hall current and injected charge current, is the figure of merit for charge-to-spin conversion efficiency. To date, measured values of θ_{sH} range from $\sim 10^{-4}$ in semiconductors to ∼0.1 in metals like β-Ta and β-W [2].

Concurrently, the discovery of graphene [4] has ignited a considerable amount of activity, owing to its unique electronic properties and versatility for practical applications, including possible applications in spintronics [5]. The intrinsically small SOC and hyperfine interactions [6] in graphene lead to spin relaxation lengths reaching several tens of micrometers at room temperature [7–10] but simultaneously making pristine graphene inactive for the SHE [5]. On the other hand, recent nonlocal transport measurements on graphene decorated with heavy adatoms like copper, gold, and silver have extracted exceptionally large values for $\theta_{sH} \sim 0.2$ [11]. These reports follow prior experiments on weakly hydrogenated graphene, which showed surprisingly similar results [12] despite using light adatoms like hydrogen. The large values of θ_{sH} observed in both types of experiments have been supported by semiclassical transport theories [13,14].

The very recent experiments [15,16] aiming to reproduce these results have indeed confirmed a large nonlocal transport signal near the charge neutral point (CNP) of graphene which, however, appears to be disconnected from SHE physics or any other spin-related mechanism. For example, Wang and co-workers [15] reported that Au- or Ir-decorated graphene exhibits no signature of the SHE and relate the large nonlocal resistance R_{NL} to the formation of neutral Hall currents. Kaverzin and van Wees [16] found large R_{NL} in hydrogenated graphene which was insensitive to an applied in-plane magnetic field. These authors [16] exclude the valley Hall effect and long-range chargeless valley currents [17] as mediating such R_{NL}, given the absence of both its temperature dependence and broken inversion symmetry, and conclude that a nontrivial and unknown phenomenon is at play.

The presently available theories for θ_{sH} [13] or R_{NL} [18] offer little guidance on how to resolve these controversies, since they utilize semiclassical approaches to charge transport and spin relaxation which are known to break down [19,20] near the CNP. Moreover, while the Kubo formula [21] offers a fully quantum-mechanical treatment that can, in principle, capture all relevant effects, its standard analytic evaluation [22] neglects terms (such as those corresponding to skew scattering from pairs of closely spaced impurities [23]) in the perturbative expansion in

 © 2016 American Physical Society

disorder strength which can become crucial for clusters of adatoms. Finally, the impact of unavoidable adatom clustering [24] on $\theta_{\rm sH}$ is an open and important question, since adatom segregation has been shown to strongly affect spin transport properties [25,26].

In this Letter, the spin Hall angle in graphene decorated with Au adatoms is computed by using two different *numerically exact* quantum transport methodologies—the real-space Kubo formula and the multiterminal Landauer-Büttiker (LB) formula [27]. At zero temperature, both methods yield $\theta_{\rm sH} \sim 0.1$–0.3 for the same Au-adatom concentration n_i. However, those values require rather large $n_i \gtrsim 10\%$ and drop significantly when temperature and adatom clustering are taken into account.

Furthermore, the LB formula applied to six-terminal graphene geometry in Fig. 1 reveals large background contributions to $R_{\rm NL}$ even when *SOC is artificially turned off*. They are, therefore, unrelated to SHE physics and are also unrelated to the trivial Ohmic contribution due to classical current paths [16,18]. We show that their sign [28,29] and scaling with the channel length L make it possible to understand their origin. This allows us to propose a novel six-terminal graphene setup—see Fig. S7 in Supplemental Material [30]—where such background contributions can be eliminated in order to study a purely SHE-driven $R_{\rm NL}$ signal.

Hamiltonian model for Au-decorated graphene.—When an adatom like gold, thallium or indium is absorbed onto a graphene surface, it resides in the center of graphene carbon rings where it can enhance the intrinsic SOC or induce Rashba SOC due to the broken inversion symmetry [34]. The minimal (with a single π orbital per site) effective tight-binding model for graphene with such adatoms is given by

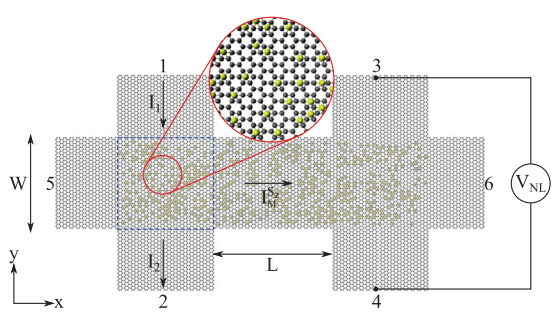

FIG. 1. Schematic view of a six-terminal graphene employed to compute the nonlocal resistance $R_{\rm NL} = V_{\rm NL}/I_1$ and the spin Hall angle $\theta_{\rm sH} = I_5^{S_z}/I_1$. For nonlocal transport, the injected transverse charge current between leads 1 and 2 generates the longitudinal spin current $I_5^{S_z}$ in lead 5 as well as the mediative spin current $I_M^{S_z}$, whose conversion into the voltage drop $V_{\rm NL} = V_3 - V_4$ between leads 3 and 4 generates $R_{\rm NL}$. The dashed region illustrates the sample of size 400 nm × 400 nm, with periodic boundary conditions, used for calculations of Kubo conductivities. The enlargement shows carbon atoms (black circles) and Au adatoms (yellow circles).

$$\mathcal{H} = -\gamma_0 \sum_{\langle ij \rangle} c_i^\dagger c_j + \frac{2i}{\sqrt{3}} V_I \sum_{\langle\langle ij \rangle\rangle \in \mathcal{R}} c_i^\dagger \vec{s} \cdot (\vec{d}_{kj} \times \vec{d}_{ik}) c_j + i V_R \sum_{\langle ij \rangle \in \mathcal{R}} c_i^\dagger \vec{z} \cdot (\vec{s} \times \vec{d}_{ij}) c_j - \mu \sum_{i \in \mathcal{R}} c_i^\dagger c_i. \quad (1)$$

The first term is the nearest-neighbor hopping term with $\gamma_0 = 2.7$ eV. The second term is the next-nearest-neighbor hopping term, which accounts for the local intrinsic SOC enhancement by adatoms residing on the set of hexagons $\mathcal{R}$. The unit vector $\vec{d}_{kj}$ points from atom j to atom k, with atom k standing in between i and j, and $\vec{s} = (s_x, s_y, s_z)$ is the vector of the Pauli matrices. The third term is the nearest-neighbor hopping term describing the Rashba SOC which explicitly violates $\vec{z} \to -\vec{z}$ symmetry. The last term is the on-site potential μ on carbon atoms in the hexagons hosting adatoms, which simulates charge modulation induced locally around the adatom [34]. The Hamiltonian in Eq. (1) has been employed to study spin dynamics in graphene decorated with Au adatoms [19], and here we use the same parameters $V_I = 0.007\gamma_0$, $V_R = 0.0165\gamma_0$, and $\mu = 0.1\gamma_0$ fitted to first-principles calculations [34].

Figure 1 shows the geometry used for the calculations of bulk Kubo conductivities and multiterminal charge and spin currents. The calculations of $\theta_{\rm sH}$ with the Kubo formula are performed using a graphene flake of the size 400 nm × 400 nm enclosed in a dashed square with periodic boundary conditions. For LB calculations, we consider full six-terminal geometry in Fig. 1, where the central region with edges of armchair type, width $W = 50$ nm (composed of $3n + 2$ dimer lines, so that its electronic structure resembles that of large-area graphene [20]), and variable distance L between the pair of leads 1 and 2 and the pair of leads 3 and 4 is attached to two armchair longitudinal leads and four transverse leads with zigzag edges and of width $W = 50$ nm. Akin to the experimental procedure [11,12,15,16,35], injecting unpolarized charge current I_1 into this measurement geometry induces $R_{\rm NL} = (V_3 - V_4)/I_1$ and $\theta_{\rm sH} = I_5^{S_z}/I_1$.

Real-space Kubo formula for spin Hall conductivity.—The Kubo formula for spin Hall conductivity $\sigma_{\rm sH}$ reads [2]

$$\sigma_{\rm sH} = \frac{e\hbar}{\Omega} \sum_{m,n} \frac{f(E_m) - f(E_n)}{E_m - E_n} \frac{{\rm Im}[\langle m|J_x^z|n\rangle\langle n|v_y|m\rangle]}{E_m - E_n + i\eta}, \quad (2)$$

where v_x is the velocity operator and $J_x^z = (\hbar/4)\{s_z, v_x\}$ is the spin-current operator. The numerical evaluation of Eq. (2) is usually made by finding the whole spectrum E_m and the full set of eigenvectors $\{|m\rangle\}$ of $\mathcal{H}$, which is a computationally expensive task. Here we develop an alternative and efficient real-space formalism by rewriting $\sigma_{\rm sH}$ as

$$\sigma_{\rm sH} = \frac{e\hbar}{\Omega} \int dxdy \frac{f(x) - f(y)}{(x-y)^2 + \eta^2} j(x,y), \quad (3)$$

with $j(x,y)=\sum_{m,n}\mathrm{Im}[\langle m|J_x^z|n\rangle\langle n|v_y|m\rangle]\delta(x-E_m)\delta(y-E_n)$. This can be calculated by rescaling $\mathcal{H}$, x, y, and E into the interval $[-1,1]$ (the corresponding variables are h, $\hat{x}$, $\hat{y}$, and ϵ, respectively) and by expanding $j(x,y)$ into Chebyshev polynomials $T_m(\hat{x})$ as $j(x,y)=\sum_{m,n}^{M}[4\mu_{mn}g_m g_n T_m(\hat{x})\times T_n(\hat{y})]/[(1+\delta_{m,0})(1+\delta_{n,0})\pi^2\sqrt{(1-\hat{x}^2)(1-\hat{y}^2)}]$, where $\mu_{mn}=\mathrm{Im}\{\mathrm{Tr}[J_x^z T_n(h) v_y T_m(h)]\}/\Delta E^2$ and ΔE is half the bandwidth [36]. Here g_m is the filter, Jackson kernel, that minimizes the Gibbs oscillations arising in truncating the series to finite order M [36]. The trace in μ_{mn} is computed by averaging [37] over a small number $r \ll N$ of random phase vectors $|\varphi\rangle$, with N being the number of carbon atoms considered in the sample. Hereafter, $M=1500$ $(=6000)$ for σ_{sH} (σ_{xx}), $r=1$, and $N=4\times10^6$. Similar methods have been developed for the longitudinal conductivity σ_{xx} [37], Hall conductivity σ_{xy} [38,39], and spin Hall conductivity σ_{sH} [40]. The method is validated by comparing our numerically evaluated σ_{sH} with analytic results [41] for clean graphene with homogeneous Rashba or intrinsic SOC [30].

Spin Hall angle for different adatom distributions.— Figure 2 shows σ_{sH} for $n_i=15\%$ of Au adatoms distributed in a scattered [Fig. 2(a)] or clustered fashion [Fig. 2(b)], where clusters are randomly distributed islands of radius $\in[1,3]$ nm. Although the random distribution of Au adatoms and the Rashba SOC associated with them induce scattering [$\mu=0.1\gamma_0$ in Eq. (1)], the dependence of σ_{sH} on the Fermi energy E_F in the absence of intrinsic SOC is reminiscent of a step behavior obtained for a homogeneous Rashba SOC [30], with $\sigma_{\mathrm{sH}}\simeq\pm e/4\pi$ near the CNP. Adding a small intrinsic SOC, $V_I=0.007\gamma_0\ll V_R$, slightly changes the absolute value of σ_{sH} but preserves the step behavior. In contrast, the clustered distribution of Au adatoms suppresses the step behavior and smooths out the shape of σ_{sH} close to the CNP. The effect of intrinsic SOC is more pronounced for the clustered distribution with a more significant enhancement of σ_{sH} on both the electron and the hole side.

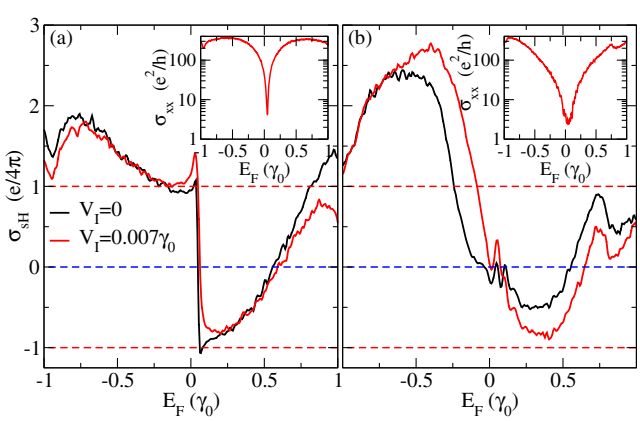

FIG. 2. Spin Hall σ_{sH} (main frame) and longitudinal σ_{xx} (insets) conductivities for the two cases of $n_i=15\%$ Au-adatom distributions: (a) scattered and (b) clustered, where Au islands have varying radius $\in[1,3]$ nm. In both cases, the effect of the presence (red lines, $V_I=0.007\gamma_0$) or absence (black lines, $V_I=0$) of the enhanced intrinsic SOC within the hexagons hosting adatoms is also shown. All results are averaged over 400 disorder configurations.

The spin Hall angle $\theta_{\mathrm{sH}}=\sigma_{\mathrm{sH}}/\sigma_{xx}$ requires the additional calculation of the longitudinal conductivity σ_{xx}, which is performed using a real-space Kubo formula [30]. Figure 2 (insets) shows σ_{xx} for both cases. Comparable values of σ_{xx} are obtained at the CNP, but for the scattered case σ_{xx} increases with energy faster than for the clustered case. Figure 3 shows θ_{sH} for $n_i=15\%$ of Au adatoms, which are distributed homogeneously (black lines) or in clusters (red line). Remarkably, the values of θ_{sH} shown in Fig. 3 are very large ~0.1–0.3 close to the CNP, which is similar to experimentally reported values [11]. At the CNP, a threefold decrease in θ_{sH} is obtained when adatoms are clustered into islands with a small radius. This conclusion seems to differ from the semiclassical transport predictions, where θ_{sH} increases with the radius of adatom clusters [13], although a strict comparison would require to treat a system consisting of identical islands. At higher energies, we observe a sizable θ_{sH} for clustered adatoms, which contrasts with vanishingly small values for the scattered geometry. We finally extrapolate that, for $n_i=2\%$–3% (as estimated in experiments [11]), θ_{sH} should range between 0.01 and 0.1 (see Supplemental Material [30]). We stress, however, that our calculations represent an upper limit for experimental situations. There, the increase of the cluster size and the finite temperature can significantly decrease θ_{sH} below 0.01 [30].

It is also instructive to compare the results in Fig. 2 to the case of heavier adatoms like thallium (Tl), which locally and substantially enhance the intrinsic SOC while generating negligible Rashba SOC [34]. A crossover from the quantum SHE to the conventional SHE has been predicted [26] when the distribution of Tl adatoms is changed from scattered to clustered. Figure S2 in Supplemental Material [30] shows that the SHE due to clustered Tl adatoms is

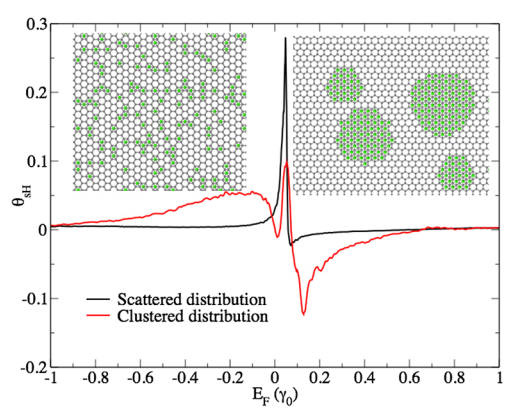

FIG. 3. Spin Hall angle $\theta_{\mathrm{sH}}=\sigma_{\mathrm{sH}}/\sigma_{xx}$ corresponding to Fig. 2 for scattered (black curve) and clustered (red curve) distributions of Au adatoms, which are illustrated in the insets.

characterized by larger θ_{sH} than in the case of either scattered or clustered Au adatoms.

Nonlocal resistance and spin Hall angle in multiterminal graphene.—In the SHE experiments [11,12], multiterminal graphene devices are employed to measure R_{NL}, as illustrated in Fig. 1. In such a circuit, a charge current I_1 injected from lead 1 towards lead 2 generates the nonlocal resistance $R_{NL} = (V_3 - V_4)/I_1$ at the Fermi energy E_F sufficiently close to the CNP. The appearance of nonzero R_{NL}, due to a SHE-driven mechanism, is explained by charge current I_1 inducing mediative spin current $I_M^{S_z}$ in the first crossbar in Fig. 1 flowing in the direction $5 \to 6$, which is subsequently converted into the nonlocal voltage $V_{NL} = V_3 - V_4$ by the inverse SHE in the second crossbar. We calculate the total charge I_p and spin $I_p^{S_z}$ currents and voltages V_p in leads $p = 2$–6 in response to injected charge current I_1 using the multiterminal LB formula [27], as implemented in the KWANT software package [30,42].

The spin Hall angle—defined as $\theta_{sH} = I_5^{S_z}/I_1$—is shown in Fig. 4(b), where we confirm large values obtained from the Kubo formula as well as the detrimental effect of clustering of Au adatoms. While both Kubo and LB formula calculations predict $\theta_{sH} \simeq 0.1$ close to the CNP, thermal broadening effects included in LB formula calculations can reduce θ_{sH} by up to one order of magnitude [see Fig. 4(b)]. By comparing Fig. 4(b) with Fig. S4 of Supplemental Material [30], we find that the hypothetical case of homogeneous Rashba SOC, due to Au adatoms covering every hexagon in Fig. 1, generates the SHE akin to the intrinsic one in finite-size two-dimensional electron gases [43,44]. Its θ_{sH} exhibits a wider peak (centered at $E_F = 0.3\gamma_0$ due to doping of graphene by Au adatoms) of smaller magnitude than in the case of randomly scattered Au adatoms. Thus, adatom-induced resonant scattering [13] plays an important role in generating a large extrinsic SHE.

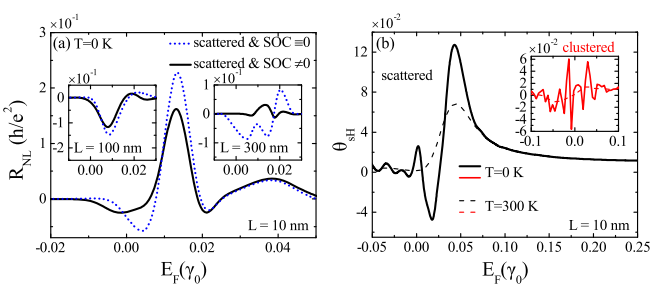

FIG. 4. (a) Nonlocal resistances for six-terminal graphene in Fig. 1 with $n_i = 15\%$ of scattered Au adatoms, fixed channel width $W = 50$ nm, and several channel lengths: $L = 10$ nm (main frame); $L = 100$ nm (left inset); and $L = 300$ nm (right inset). Dotted lines plot R_{NL} when all SOC terms in Eq. (1) are switched off (SOC $\equiv 0 \Leftrightarrow V_I = V_R = 0$). (b) Spin Hall angle, obtained from LB formula calculations, for the same concentration of Au adatoms which are scattered (main frame) or clustered (inset). All curves are averaged over ten disorder configurations.

Figure 4(a) shows R_{NL} as a function of energy and for various channel lengths L. Most notably, we find a nonzero R_{NL} *even when all SOC terms are switched off* ($V_R = V_I = 0$) in Eq. (1) while keeping random on-site potential $\mu \neq 0$ due to Au adatoms unchanged. Furthermore, we find a complex sign change of R_{NL} in Fig. 4(a) with increasing channel length from $L = 10$ nm to $L = 300$ nm, which suggests the following interpretation. The total R_{NL} can have four contributions $R_{NL} = R_{NL}^{SHE} + R_{NL}^{Ohm} + R_{NL}^{qb} + R_{NL}^{pd}$, assuming they are additive after disorder averaging. For an unpolarized charge current injected from lead 1 (i.e., electrons injected from lead 2): R_{NL}^{SHE} generated by the combined direct and inverse SHE has a positive sign; trivial Ohmic contribution R_{NL}^{Ohm} due to classical diffusive charge transport [16,18] has a positive sign; R_{NL}^{qb} is the negative quasiballistic contribution arising due to direct transmission $T_{32} \neq 0$ from lead 2 to lead 3 (see Fig. S6 in Supplemental Material [30]), as observed previously in SHE experiments on multiterminal gold devices [28]; finally, R_{NL}^{pd} is a positive contribution specific to Dirac materials where evanescent wave functions generate pseudodiffusive transport [45] close to the CNP characterized by two-terminal conductance scaling as $G \propto 1/L$ even in perfectly clean samples as long as their geometry satisfies $W > L$ (see Fig. S5 in Supplemental Material [30]).

Thus, in a device with $W > L$, such as $W = 50$ nm and $L = 10$ nm in the main frame of Fig. 4(a), the positive sign R_{NL} is dominated by R_{NL}^{pd}, which can be larger than in the case of perfectly clean graphene in Fig. S5 of Supplemental Material [30] due to scattering from impurities (of uniform strength) at the CNP [46]. The negative sign of R_{NL} in the two insets in Fig. 4(a) in the absence of SOC and for $L > W$ suggests that R_{NL}^{Ohm} can be safely neglected in our samples due to small n_i—we estimate the mean free path $\ell =$ 300–400 nm for $n_i = 15\%$, so that when diffusive transport regime sets in for $\ell < L$, the Ohmic contribution $R_{NL}^{Ohm} \propto \exp(-\pi L/W)$ [16,18] is already negligible due to $L/W \gg 1$. Therefore, for $L > W$ the main competition is between R_{NL}^{qb} with a negative sign and R_{NL}^{SHE} with a positive sign, as found in the two insets in Fig. 4(a). The existence of background contributions to R_{NL} that do not originate from the SHE, and can be even larger than R_{NL}^{SHE}, could explain the insensitivity of the total R_{NL} to the applied external in-plane magnetic field observed in some experiments [15,16].

The difficulty in clarifying the dominant contribution to R_{NL} could be resolved by detecting its sign change as a function of the channel length L in Fig. 1. An alternative is to design a setup where R_{NL}^{Ohm}, R_{NL}^{qb}, and R_{NL}^{pd} are negligible so that R_{NL}^{SHE} can be isolated. We propose such a setup in Fig. S7 of Supplemental Material [30], where adatoms are removed in the channel. When such a channel is sufficiently long, $R_{NL}^{pd} = 0$ due to $L > W$ and R_{NL}^{Ohm}, $R_{NL}^{qb} \to 0$ due to the absence of impurity scattering in the channel, so that

mediative spin current $I_M^{S_z}$ generated by the direct SHE in the first crossbar arrives conserved [44] at the second crossbar where it is converted into V_{NL} by the inverse SHE. Indeed, Fig. S8 of Supplemental Material [30] demonstrates that R_{NL} and θ_{sH} in this setup are unambiguously related, since they both display a sharp peak at virtually the same E_F very close to the CNP.

A. W. Cummings and J. H. Garcia are acknowledged for critical reading of the manuscript. This project has received funding from the European Union's Horizon 2020 research and innovation programme under grant agreement No. 696656. S. R. acknowledges Funding from the Spanish Ministry of Economy and Competitiveness and the European Regional Development Fund (Project No. FIS2015-67767-P (MINECO/FEDER)), the Secretaria de Universidades e Investigación del Departamento de Economía y Conocimiento de la Generalidad de Cataluña, and the Severo Ochoa Program (MINECO, Grant No. SEV-2013-0295). We acknowledge computational resources from PRACE and the Barcelona Supercomputing Center (Mare Nostrum), under Project No. 2015133194. J. M. M.-T. was supported as a Fulbright Colombia Scholar and by Colciencias (Departamento Administrativo de Ciencia, Tecnologia e Innovacion) of Colombia. B. K. N. was supported by United States National Science Foundation (NSF) Grant No. ECCS 1509094 and is grateful for the hospitality of Centre de Physique Théorique de Grenoble-Alpes where part of this work was done. S. O. V. acknowledges support from the European Research Council under Grant Agreement No. 308023 SPINBOUND. The supercomputing time was provided by Extreme Science and Engineering Discovery Environment (XSEDE), which is supported by NSF Grant No. ACI-1053575.

*bnikolic@udel.edu
†stephan.roche@icn2.cat

[1] G. Vignale, J. Supercond. Novel Magn. **23**, 3 (2010).
[2] J. Sinova, S. O. Valenzuela, J. Wunderlich, C. H. Back, and T. Jungwirth, Rev. Mod. Phys. **87**, 1213 (2015).
[3] Y. Kato, R. C. Myers, A. C. Gossard, and D. D. Awschalom, Science **306**, 1910 (2004); J. Wunderlich, B. Kaestner, J. Sinova, and T. Jungwirth, Phys. Rev. Lett. **94**, 047204 (2005); S. O. Valenzuela and M. Tinkham, Nature (London) **442**, 176 (2006); E. Saitoh, M. Ueda, H. Miyajima, and G. Tatara, Appl. Phys. Lett. **88**, 182509 (2006).
[4] A. H. Castro Neto, F. Guinea, N. M. R. Peres, K. S. Novoselov, and A. K. Geim, Rev. Mod. Phys. **81**, 109 (2009); A. Ferrari *et al.*, Nanoscale **7**, 4598 (2015).
[5] S. Roche *et al.*, 2D Mater. **2**, 030202 (2015).W. Han, R. K. Kawakami, M. Gmitra, and J. Fabian, Nat. Nanotechnol. **9**, 794 (2014);
[6] D. Huertas-Hernando, F. Guinea, and A. Brataas, Phys. Rev. B **74**, 155426 (2006); M. Gmitra, S. Konschuh, C. Ertler, C. Ambrosch-Draxl, and J. Fabian, Phys. Rev. B **80**, 235431 (2009); A. H. Castro Neto and F. Guinea, Phys. Rev. Lett. **103**, 026804 (2009); V. K. Dugaev, E. Ya. Sherman, and J. Barnas, Phys. Rev. B **83**, 085306 (2011).
[7] N. Tombros, C. Jozsa, M. Popinciuc, H. T. Jonkman, and B. J. Van Wees, Nature (London) **448**, 571 (2007).
[8] K. Pi, W. Han, K. M. McCreary, A. G. Swartz, Y. Li, and R. K. Kawakami, Phys. Rev. Lett. **104**, 187201 (2010).
[9] B. Dlubak *et al.*, Nat. Phys. **8**, 557 (2012).
[10] M. H. D. Guimarães, P. J. Zomer, J. Ingla-Aynes, J. C. Brant, N. Tombros, and B. J. van Wees, Phys. Rev. Lett. **113**, 086602 (2014); M. Drögeler, F. Volmer, M. Wolter, B. Terres, K. Watanabe, T. Taniguchi, G. Güntherodt, C. Stampfer, and B. Beschoten, Nano Lett. **14**, 6050 (2014); M. Venkata Kamalakar, C. Groenveld, A. Dankert, and S. P. Dash, Nat. Commun. **6**, 6766 (2015); B. Raes, J. E. Scheerder, M. V. Costache, F. Bonell, J. F. Sierra, J. Cuppens, J. Van de Vondel, and S. O. Valenzuela, Nat. Commun. **7**, 11444 (2016).
[11] J. Balakrishnan *et al.*, Nat. Commun. **5**, 4748 (2014).
[12] J. Balakrishnan, G. K. Wai Koon, M. Jaiswal, A. H. Castro Neto, and B. Özyilmaz, Nat. Phys. **9**, 284 (2013).
[13] A. Ferreira, T. G. Rappoport, M. A. Cazalilla, and A. H. Castro Neto, Phys. Rev. Lett. **112**, 066601 (2014).
[14] H.-Y. Yang, C. Huang, H. Ochoa, and M. A. Cazalilla, Phys. Rev. B **93**, 085418 (2016).
[15] Y. Wang, X. Cai, J. Reutt-Robey, and M. S. Fuhrer, Phys. Rev. B **92**, 161411 (2015).
[16] A. A. Kaverzin and B. J. van Wees, Phys. Rev. B **91**, 165412 (2015).
[17] R. V. Gorbachev *et al.*, Science **346**, 448 (2014).
[18] D. A. Abanin, A. V. Shytov, L. S. Levitov, and B. I. Halperin, Phys. Rev. B **79**, 035304 (2009).
[19] D. V. Tuan, F. Ortmann, D. Soriano, S. O. Valenzuela, and S. Roche, Nat. Phys. **10**, 857 (2014); D. V. Tuan, F. Ortmann, A. W. Cummings, D. Soriano, and S. Roche, Sci. Rep. **6**, 21046 (2016); D. Van Tuan and S. Roche, Phys. Rev. Lett. **116**, 106601 (2016).
[20] C.-L. Chen, C.-R. Chang, and B. K. Nikolić, Phys. Rev. B **85**, 155414 (2012).
[21] P. Středa, J. Phys. C **15**, L717 (1982).
[22] N. A. Sinitsyn, J. E. Hill, H. Min, J. Sinova, and A. H. MacDonald, Phys. Rev. Lett. **97**, 106804 (2006).
[23] I. A. Ado, I. A. Dmitriev, P. M. Ostrovsky, and M. Titov, Phys. Rev. Lett. **117**, 046601 (2016); M. Milletari and A. Ferreira, Phys. Rev. B **94**, 134202 (2016).
[24] E. Sutter, P. Albrecht, B. Wang, M.-L. Bocquet, L. Wu, Y. Zhu, and P. Sutter, Surf. Sci. **605**, 1676 (2011).
[25] K. Pi, K. M. McCreary, W. Bao, W. Han, Y. F. Chiang, Y. Li, S.-W. Tsai, C. N. Lau, and R. K. Kawakami, Phys. Rev. B **80**, 075406 (2009); M. I. Katsnelson, F. Guinea, and A. K. Geim, Phys. Rev. B **79**, 195426 (2009); K. M. McCreary, K. Pi, A. G. Swartz, W. Han, W. Bao, C. N. Lau, F. Guinea, M. I. Katsnelson, and R. K. Kawakami, Phys. Rev. B **81**, 115453 (2010).
[26] A. Cresti, D. Van Tuan, D. Soriano, A. W. Cummings, and S. Roche, Phys. Rev. Lett. **113**, 246603 (2014).
[27] M. Büttiker, Phys. Rev. Lett. **57**, 1761 (1986).
[28] G. Mihajlović, J. E. Pearson, M. A. Garcia, S. D. Bader,
and A. Hoffmann, Phys. Rev. Lett. **103**, 166601 (2009).
[29] Z. Wang, H. Liu, H. Jiang, and X. C. Xie, Phys. Rev. B **94**, 035409 (2016).

[30] See Supplemental Material (which includes Refs. [31–33]) at http://link.aps.org/supplemental/10.1103/PhysRevLett.117.176602 for details on the validation tests of our real-space Kubo formula for σ_{sH}; comparison of θ_{sH} for Au vs Tl adatoms; and LB formula calculations of R_{NL} and θ_{sH} on additional clean and disordered multiterminal graphene geometries.

[31] C. L. Kane and E. J. Mele, Phys. Rev. Lett. **95**, 226801 (2005).

[32] L. Sheng, D. N. Sheng, C. S. Ting, and F. D. M. Haldane, Phys. Rev. Lett. **95**, 136602 (2005).

[33] K. Kazymyrenko and X. Waintal, Phys. Rev. B **77**, 115119 (2008); M. Wimmer and K. Richter, J. Comput. Phys. **228**, 8548 (2009).

[34] C. Weeks, J. Hu, J. Alicea, M. Franz, and R. Wu, Phys. Rev. X **1**, 021001 (2011).

[35] A. Avsar, J. H. Lee, G. K. Wai Koon, and B. Özyilmaz, 2D Mater. **2**, 044009 (2015).

[36] A. Weisse, G. Wellein, A. Alvermann, and H. Fehske, Rev. Mod. Phys. **78**, 275 (2006).

[37] S. Roche and D. Mayou, Phys. Rev. Lett. **79**, 2518 (1997); S. Roche, Phys. Rev. B **59**, 2284 (1999); A. Ferreira and E. R. Mucciolo, Phys. Rev. Lett. **115**, 106601 (2015).

[38] F. Ortmann and S. Roche, Phys. Rev. Lett. **110**, 086602 (2013); F. Ortmann, N. Leconte, and S. Roche, Phys. Rev. B **91**, 165117 (2015).

[39] J. H. Garcia, L. Covaci, and T. G. Rappoport, Phys. Rev. Lett. **114**, 116602 (2015).

[40] T. L. van den Berg, L. Raymond, and A. Verga, Phys. Rev. B **84**, 245210 (2011); J. H. Garcia and T. G. Rappoport, 2D Mater. **3**, 024007 (2016).

[41] A. Dyrdal, V. K. Dugaev, and J. Barnas, Phys. Rev. B **80**, 155444 (2009).

[42] C. W. Groth, M. Wimmer, A. R. Akhmerov, and X. Waintal, New J. Phys. **16**, 063065 (2014).

[43] B. K. Nikolić, L. P. Zârbo, and S. Souma, Phys. Rev. B **72**, 075361 (2005); L. Sheng, D. N. Sheng, and C. S. Ting, Phys. Rev. Lett. **94**, 016602 (2005); B. K. Nikolić and R. L. Dragomirova, Semicond. Sci. Technol. **24**, 064006 (2009).

[44] B. K. Nikolić, L. P. Zârbo, and S. Souma, Phys. Rev. B **73**, 075303 (2006).

[45] J. Tworzydło, B. Trauzettel, M. Titov, A. Rycerz, and C. W. J. Beenakker, Phys. Rev. Lett. **96**, 246802 (2006); P.-H. Chang, F. Mahfouzi, N. Nagaosa, and B. K. Nikolić, Phys. Rev. B **89**, 195418 (2014).

[46] M. Titov, Europhys. Lett. **79**, 17004 (2007).

Supplemental Material for "Spin Hall Effect and Origins of Nonlocal Resistance in Adatom-Decorated Graphene"

D. Van Tuan,[1,2] J. M. Marmolejo-Tejada,[3,4] X. Waintal,[5] B. K. Nikolić,[3,*] S. O. Valenzuela,[1,6] and S. Roche[1,6,†]

[1] *Catalan Institute of Nanoscience and Nanotechnology (ICN2), CSIC and The Barcelona Institute of Science and Technology, Campus UAB, Bellaterra, 08193 Barcelona, Spain*
[2] *Department of Electrical and Computer Engineering, University of Rochester, Rochester, NY 14627, USA*
[3] *Department of Physics and Astronomy, University of Delaware, Newark, DE 19716-2570, USA*
[4] *School of Electrical and Electronics Engineering, Universidad del Valle, Cali, AA 25360, Colombia*
[5] *CEA-INAC/UJF Grenoble 1, SPSMS UMR-E 9001, Grenoble F-38054, France*
[6] *ICREA–Institució Catalana de Recerca i Estudis Avançats, 08010 Barcelona, Spain*

In this Supplemental Material, we include more details about the real-space Kubo formula for the longitudinal charge conductivity σ_{xx}, as well as two validation tests for our implementation of the real-space Kubo formula for the spin Hall conductivity $\sigma_{\rm sH}$. We also include additional results for the nonlocal resistance $R_{\rm NL}$—computed using multiterminal Landauer-Büttiker (LB) formula [1] implemented in `KWANT` software package [2]—in several different six-terminal clean and disordered graphene geometries which complement setup considered in Fig. 1 of the main text.

I. CHEBYSHEV-POLYNOMIAL GREEN FUNCTION METHOD FOR KUBO FORMULA

The longitudinal conductivity is calculated using a method similar to the one developed in the main text for $\sigma_{\rm sH}$ called Chebyshev-polynomial Green function method. This method was introduced very recently by Ferreira and Mucciolo [3] to study charge transport in graphene flakes containing very large number of carbon atoms and disorder due to structural vacancies. It is inspired from the real-space order-N quantum transport method pioneered in Refs. [4]. The starting point is to write an exact representation of the Kubo formula for the zero-frequency conductivity

$$\sigma_{xx}(E,\eta) = \frac{2\hbar e^2}{\pi\Omega}\sum_{m,n=0}^{M} \mathrm{Im}\left[g_m\left(\frac{E+i\eta}{\Delta E}\right)\right]\mathrm{Im}\left[g_n\left(\frac{E+i\eta}{\Delta E}\right)\right]\mu_{mn}, \tag{1}$$

where

$$\mu_{mn} = \frac{1}{\Delta E^2}\mathrm{Tr}\left[v_x T_m\left(\frac{\mathcal{H}}{\Delta E}\right) v_x T_n\left(\frac{\mathcal{H}}{\Delta E}\right)\right], \tag{2}$$

is given in terms of the velocity operator $v_x = [x,\mathcal{H}]/i\hbar$ and Chebyshev polynomials $T_n(\mathcal{H}/\Delta E)$. Here Ω is the area, ΔE is half the bandwidth and η is the inelastic broadening parameter, required to define the retarded Green function $\mathcal{G}(E+i\eta)$, which has to be larger than the mean level spacing. The coefficients $g_m((E+i\eta)/\Delta E)$ appear in the expansion of $\mathcal{G}(E+i\eta)$ in terms of first-kind Chebyshev polynomials [3]

$$\mathcal{G}(E+i\eta) = \frac{1}{E+i\eta-\mathcal{H}} = \frac{1}{\Delta E}\sum_{m=0}^{\infty} g_m\left(\frac{E+i\eta}{\Delta E}\right) T_m\left(\frac{\mathcal{H}}{\Delta E}\right), \tag{3}$$

and are given by

$$g_m(z) = \frac{2}{i}\frac{1}{1+\delta_{m,0}}\frac{\left(z-i\sqrt{1-z^2}\right)^m}{\sqrt{1-z^2}}. \tag{4}$$

The most time-consuming part of this method is evaluation of the trace in Eq. (2), which for sparse matrices representing the tight-binding effective Hamiltonian $\mathcal{H}$ can be replaced by stochastic average over r complex vectors

*Electronic address: `bnikolic@udel.edu`
†Electronic address: `stephan.roche@icn2.cat`

with random phases [3]. For example, insets of Fig. 2 in the main text show σ_{xx} for $n_i = 15\%$ concentration of Au adatoms on graphene where we used Hamiltonian matrix of size $N = 4 \times 10^6$ (i.e., N is the number of carbon atoms considered in the dashed square in Fig. 1 of the main text), $M = 6000$ and all results are averaged over 400 disorder configurations.

II. VALIDATION OF THE REAL-SPACE METHOD FOR SPIN HALL CONDUCTIVITY

To validate our implementation of the real-space Kubo formula for $\sigma_{\rm sH}$, we perform calculations for graphene with homogeneous spin-orbit couplings (SOCs) as described by the Hamiltonian

$$\mathcal{H} = -\gamma_0 \sum_{\langle ij \rangle} c_i^\dagger c_j + \frac{2i}{\sqrt{3}} V_I \sum_{\langle\langle ij \rangle\rangle} c_i^\dagger \vec{s} \cdot (\vec{d}_{kj} \times \vec{d}_{ik}) c_j + i V_R \sum_{\langle ij \rangle} c_i^\dagger \vec{z} \cdot (\vec{s} \times \vec{d}_{ij}) c_j. \tag{5}$$

Here the symbols have the same meaning as in Eq. (1) of the main text, except that V_I and V_R are nonzero on every hexagon. In the continuum limit and close to K and K' points located at the corners of the first Brillouin zone of graphene, this Hamiltonian is equivalent to the Dirac Hamiltonian

$$H(\vec{k}) = \hbar v_F \vec{\sigma} \cdot \vec{k} + \lambda_I \sigma_z s_z + \lambda_R \left(\vec{\sigma} \times \vec{s}\right)_z, \tag{6}$$

with $\lambda_R = 3V_R/2$ and $\lambda_I = 3\sqrt{3}V_I$.

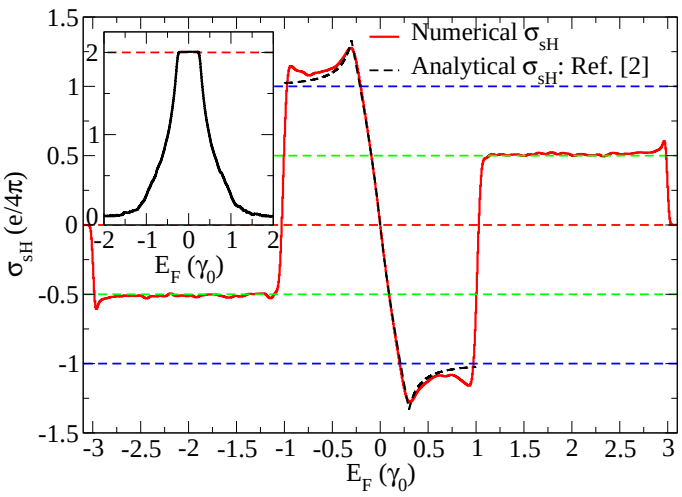

Fig. S1: Main frame: Spin Hall conductivity $\sigma_{\rm sH}$ of graphene with homogeneous Rashba SOC obtained from our real-space Kubo formula calculations (red solid line)—with parameters $V_R = 0.1\gamma_0$, $M = 300$, $r = 100$ and $N = 1.3 \times 10^6$—is compared with analytic expression (black dashed line) in Eq. (7). Inset: Numerically computed $\sigma_{\rm sH}$ for the case of homogeneous intrinsic SOC with parameters: $V_I = 0.05\gamma_0$, $M = 500$, $r = 50$ and $N = 32 \times 10^6$.

In the first validation test, we use Hamiltonian in Eq. (5) with homogeneous Rashba SOC, $V_R = 0.1\gamma_0$, and zero intrinsic SOC, $V_I = 0$. For this case, an analytic expression [5]

$$\sigma_{\rm sH}(E) = \begin{cases} -\frac{e}{4\pi} \frac{{\rm sign}(E) E^2}{\left(E^2 - \lambda_R^2\right)} & \text{for } |E| \geq 2\lambda_R, \\ -\frac{e}{4\pi} \frac{E(E + 2{\rm sign}(E)\lambda_R)}{2\lambda_R(E + {\rm sign}(E)\lambda_R)} & \text{for } |E| < 2\lambda_R, \end{cases} \tag{7}$$

was obtained in Ref. [6] by starting from the Dirac Hamiltonian in Eq. (6). Figure S1 (main frame) compares our numerical result for $\sigma_{\rm sH}$ (red solid line) with Eq. (7) (black dashed line). Our numerical result is in perfect agreement with Eq. (7) up to $E \simeq 0.5\gamma_0$, despite the fact that Dirac Hamiltonian is expected to be a good approximation only sufficiently close to charge neutral point (CNP) at $E_F = 0$. For very small Rashba SOC, $\lambda_R \ll E$, Eq. (7) can be

rewritten as $\sigma_{\rm sH}(E) = -{\rm sign}(E)e/4\pi$, which is a step function explaining the shape of $\sigma_{\rm sH}$ in the scattered case (with $V_I = 0$) in Fig. 2(a) of the main text.

In the second validation test, we use Hamiltonian in Eq. (5) with homogeneous intrinsic SOC, $V_I = 0.05\gamma_0$, and zero Rashba SOC, $V_R = 0$. Such system exhibits quantum spin Hall effect (QSHE) with a gap opening in the bulk and two gapless helical edge states with opposite spin and momentum direction on each edge [7]. Consequently, QSHE is characterized by $\sigma_{\rm sH} = 2 \times e/4\pi$ [6–8]. Figure S1 (inset) shows our numerical result for $\sigma_{\rm sH}$ which exhibits quantized value inside the gap, which is in full accord with QSHE phenomenology.

III. SPIN HALL EFFECT IN GRAPHENE WITH CLUSTERING OF THALLIUM ADATOMS

It is insightful to compare our predictions in the main text for the SHE in graphene decorated with Au adatoms with the onset of SHE found in the case graphene decorated with clusters of thallium (Tl) adatoms [9]. Heavy adatoms like Tl locally enhance the intrinsic SOC while generating negligible Rashba SOC [10]. For large concentration and scattered distribution of Tl adatoms, QSHE is expected [10], followed by a crossover from QSHE to SHE upon Tl clustering [9]. Figure S2 shows that for clustered Tl adatoms, $\theta_{\rm sH}$ is larger than in the case of scattered Au adatoms, assuming the same concentration for both types of adatoms. Thus, high charge-to-spin conversion efficiency could be achieved by using adatoms which locally enhance intrinsic SOC, even in the presence of adatom clustering.

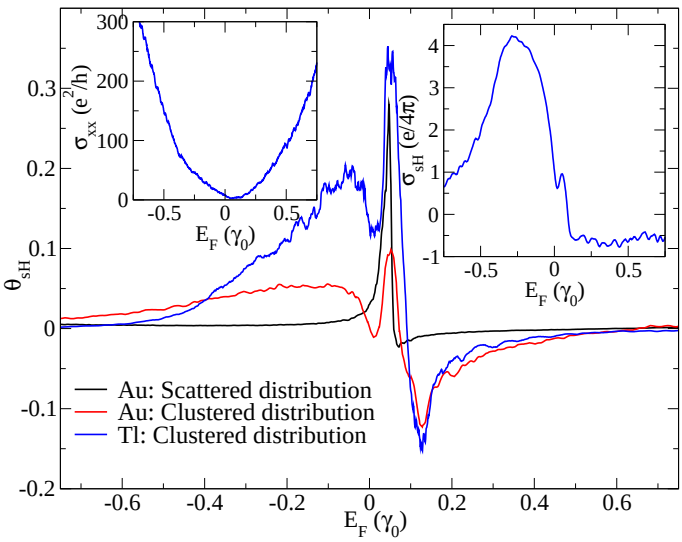

Fig. S2: Main frame: Spin Hall angle $\theta_{\rm sH}$ for graphene with Au adatoms, which are scattered (black) or clustered (red), as well as for clustered Tl adatoms (blue curve). The concentration of both Au and Tl adatoms is $n_i = 15\%$. Insets: Conductivities $\sigma_{\rm sH}$ (right inset) and σ_{xx} (left inset) for graphene with Tl adatoms whose ratio gives $\theta_{\rm sH} = \sigma_{\rm sH}/\sigma_{xx}$ in the main frame. All curves are obtained using real-space Kubo formula calculations averaged over 400 disorder configurations.

IV. SCALING OF SPIN HALL ANGLE WITH ADATOM CONCENTRATION

In the experiments [11], the density of gold clusters of diameter ranging from 20 to 40 nm is estimated to lie within $10^{10}{\rm cm}^{-2}$–$10^{11}{\rm cm}^{-2}$. This leads to $n_i \simeq 2$–3% assuming that clusters are two-dimensional. In the main text, the values of $\theta_{\rm sH}$ obtained from the Kubo formula calculations assume larger adatom concentration $n_i = 15\%$. Because of too large mean free paths (above the micrometer) for few percent adatom densities, we cannot (within our present computational capability) reach the diffusive regime in which the Kubo conductivities could be safely estimated. An estimate of $\theta_{\rm sH}$ for much lower density is actually not straightforward because the scaling of $\sigma_{\rm sH}$ with n_i is predicted to ultimately depend on the mechanism dominating the SHE [13].

Neglecting localization effects, the scaling of longitudinal conductivity should follow the Fermi golden rule, $\sigma_{xx} \sim 1/n_i$. Similarly, the spin Hall conductivity follows $\sigma_{\rm sH} \sim 1/n_i$, but only when the skew-scattering mechanism predominates the extrinsic SHE [12, 13] (e.g., as confirmed numerically in Ref. [15] for adatoms inducing Rashba SOC). As discussed in Refs. [13], $\sigma_{\rm sH}$ should be dominated by a n_i-independent value for the quantum side-jump

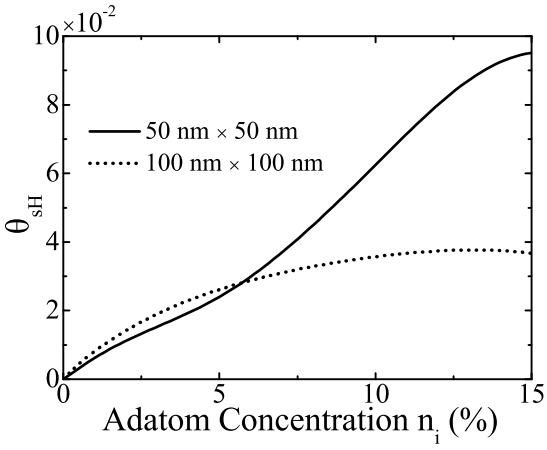

Fig. S3: Spin Hall angle as a function of the concentration of randomly scattered Au adatoms. These results are obtained from the LB formula (see Sec. V) applied to four-terminal graphene devices whose central square-shaped region of the size 50 nm × 50 nm or 100 nm × 100 nm is attached to four semi-infinite leads of the same respective width. The values of $\theta_{\rm sH}$ are averaged over the Fermi energy interval $[-0.01\gamma_0, 0.01\gamma_0]$.

mechanism, whereas higher order quantum interference terms between scattering paths could lead to n_i^α dependence (where $\alpha = 1, 2, ...$) [12–14].

Therefore in the limit of small n_i, $\theta_{\rm sH}$ is expected to be either constant or $\propto n_i$ ($\propto n_i^{\alpha+1}$). The value $n_i = 15\%$ used in our Kubo formula calculations lies outside the dilute adatom regime where such theories have been developed [13, 15], but based on the arguments above we extrapolate that for few percent of Au adatom concentration, the maximum value should range within $\theta_{\rm sH} \simeq 0.01$–$0.1$, where the lower limit is for adatom clusters. Thus, our estimate is about one order of magnitude lower than the value reported in Ref. [11]. Finite temperatures and larger clusters will lead to even lower spin Hall angles.

Finally, a brute-force calculation of $\theta_{\rm sH}$ for *arbitrary* adatom concentration in finite-size samples is possible using the multiterminal LB formula approach discussed in Sec. V. Figure S3 shows that $\theta_{\rm sH}$ does increase with the adatom concentration in the limit of low n_i, with values agreeing with estimates made above. Comparing our results in Fig. S3 with those in Refs. [13, 15] suggests that side jump and anomalous quantum processes could dominate the physics of SHE in graphene decorated with low concentration of adatoms.

V. SPIN HALL ANGLE AND NONLOCAL RESISTANCE FROM MULTITERMINAL LANDAUER-BÜTTIKER FORMULA

Our numerically exact quantum transport calculations for multiterminal finite-size graphene are based on the LB formula [1]

$$I_p = \sum_q G_{pq}(V_p - V_q). \tag{8}$$

which relates the total charge current I_p, flowing through semi-infinite ideal (i.e., without any impurities or SOC) lead p =1–6 attached to the central phase-coherent region, to voltages V_q in all other leads. The charge conductance coefficients

$$G_{pq} = \frac{e^2}{h} \int dE \, {\rm Tr}[\mathbf{t}_{pq}\mathbf{t}_{pq}^\dagger] \left(-\frac{\partial f}{\partial E}\right), \tag{9}$$

are expressed in terms of the transmission matrix $\mathbf{t}_{pq}$ between transverse propagating modes within semi-infinite leads p and q. The same Eq. (8) can be converted into the formula for total spin current $I_p^{S_\alpha}$ (which is conserved along the leads without SOC or other spin-flip mechanisms [16], as assumed in Fig. 1 of the main text)

$$I_p^{S_\alpha} = \sum_q G_{pq}^{S_\alpha}(V_p - V_q). \tag{10}$$

on the proviso that G_{pq} is replaced by the spin conductance coefficients

$$G_{pq}^{S_\alpha} = \frac{e^2}{h} \int dE \, \mathrm{Tr}[s_\alpha \mathbf{t}_{pq} \mathbf{t}_{pq}^\dagger] \left(-\frac{\partial f}{\partial E} \right), \tag{11}$$

where s_α is the Pauli matrix. The derivative of the Fermi function $(-\partial f/\partial E)$ takes into account thermal broadening effects, but inclusion of inelastic scattering at finite temperature which smooths out features of G_{pq} or $G_{pq}^{S_\alpha}$ due quantum interference effects requires to add phenomenological dephasing [17] which we do not perform in this study.

The calculation of spin and charge conductance coefficients in Eqs. (9) and (11) was performed by using `KWANT` package [2] which employs highly efficient and robust algorithms to calculate the transmission matrix, while being able to significantly outperform commonly used recursive GF methods [18] for multiterminal devices containing large number of atoms. The `KWANT` package also avoids instabilities that occur with many commonly used algorithms (such as in dealing with the evanescent modes of complicated leads) [2].

One can apply Eqs. (8) and (10) to six-terminal device in Fig. 1 of the main text by either setting the voltages V_q to find currents I_p and $I_p^{S_\alpha}$, or fix the injected current I_p or $I_p^{S_\alpha}$, and then find voltages V_q which develops as the response to it. For the analysis of experiments reported in Ref. [11] the latter approach is the most suitable, so we set injected charge current I_1 through lead 1 and current $-I_1$ flows through lead 2 while $I_p \equiv 0$ in the other four leads. We then compute voltages which develop in the leads p =3–6 in response to injected current I_1 and obtain the nonlocal resistance as the quantity which is measured directly in experiments from $R_{\mathrm{NL}} = (V_3 - V_4)/I_1$. We define the spin Hall angle for six-terminal graphene device in Fig. 1 of the main text or for device in Fig. S7 as $\theta_{\mathrm{sH}} = I_5^{S_z}/I_1$ (which is not directly measurable quantity due to difficulty in measuring spin currents $I_p^{S_\alpha}$).

A. Nonlocal resistance for a uniform distribution of gold adatoms

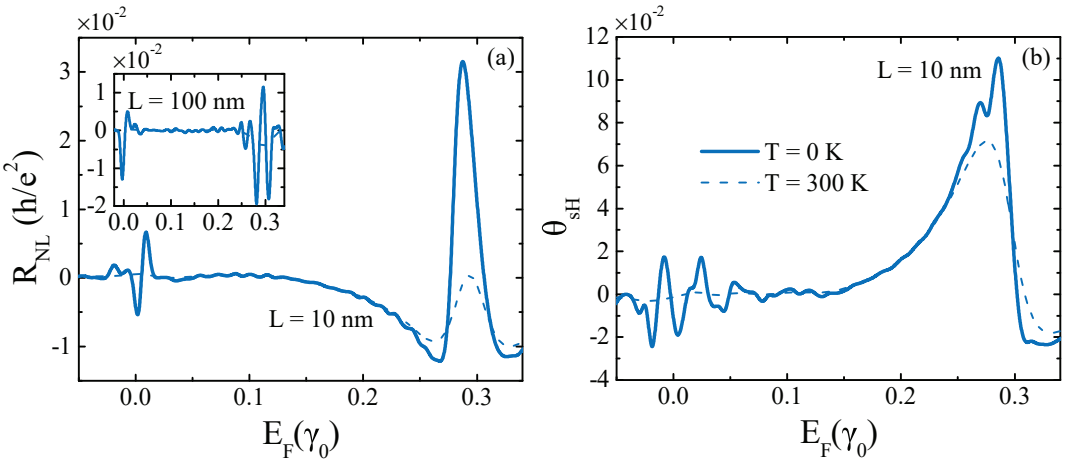

Fig. S4: (a) Nonlocal resistance R_{NL} and (b) spin Hall angle θ_{sH} as a function of the Fermi energy for graphene with uniform distribution of adatoms where every hexagon within the central region in Fig. 1 of the main text is covered by one gold adatom.

Figure S4 shows R_{NL} and θ_{sH} for the case of a completely uniform distribution of Au adatoms, where each hexagon within the central region hosts one Au adatom. Both quantities are calculated at temperatures $T = 0$ K and $T = 300$ K, where the latter includes thermal broadening effects in the LB calculations. The uniform Rashba SOC generates the intrinsic SHE in multiterminal systems, akin to the one found in multiterminal two-dimensional electron gases [16, 19, 20]. Note that large value of the nonlocal signal and θ_{sH} is observed in Fig. S4 away from CNP due to doping of graphene by $\mu = 0.3\gamma_0$ (chosen by viewing the central region of the device as a single large cluster) in Eq. (1) of the main text. The spin Hall angle and R_{NL} due to such intrinsic SHE are actually smaller than the same quantities shown in Fig. S8 for scattered distribution of Au adatoms in purely SHE-driven nonlocal transport setup in Fig. S7. This confirms the importance of resonant scattering off adatoms for enhancing the extrinsic SHE—a conclusion reached also by semiclassical transport theories [12].

B. Scaling of pseudodiffusive and quasiballistic contributions to $R_{\rm NL}$

Figure S5 shows the scaling of $R_{\rm NL}$ with the length L (at fixed width W) of six-terminal pristine graphene devices when all adatoms are removed from the setup in Fig. 1 of the main text. Such nonlocal signal, which is positive around CNP, is specific to Dirac electron systems, like graphene [21] or metallic surfaces of three-dimensional topological insulators [22], where evanescent wavefunctions penetrate through the zero gap of the Dirac cone to generate the so-called "pseudodiffusive" transport close to CNP. The pseudodiffusive transport regime is characterized by the Ohmic-like two-terminal conductance $G \propto 1/L$ [21, 22], even though the device is perfectly clean. This mechanism provides background contribution $R_{\rm NL}^{\rm pd}$ of positive sign to total $R_{\rm NL}$, as long as $W > L$, which can be further enhanced at CNP by scattering from impurities of uniform strength [23] as observed in Fig. 4(a) in the main text.

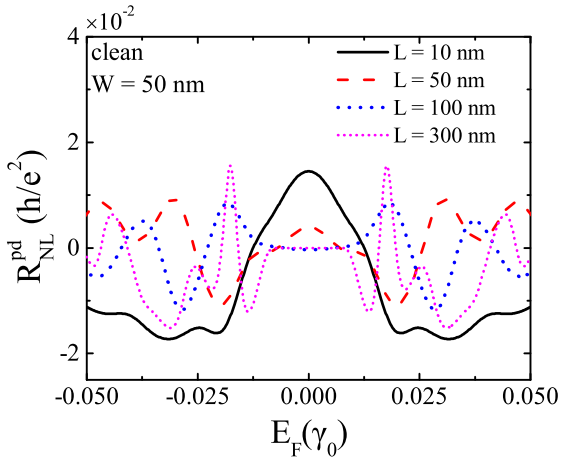

Fig. S5: Nonlocal resistance generated in perfectly clean six-terminal graphene device where all adatoms removed. The width of the device is fixed at $W = 50$ nm, while the length between the two crossbars varies from $L = 10$ nm to $L = 300$ nm.

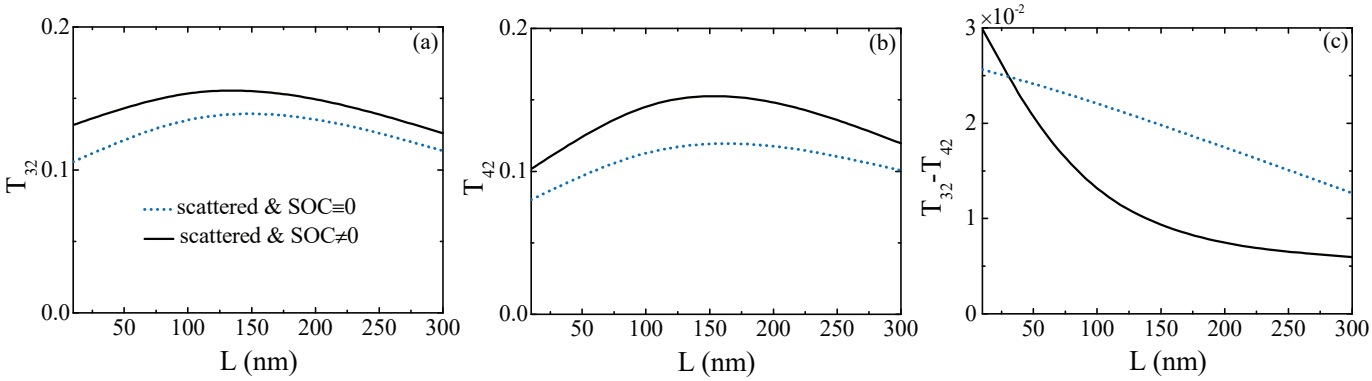

Fig. S6: Scaling with the length L of the transmission functions T_{pq} from lead q to lead p in six-terminal graphene device of width $W = 50$ nm in Fig. 1 in the main text: (a) T_{32}; (b) T_{42}; and (c) their difference, $T_{32} - T_{42}$. The central region is covered by scattered distribution of Au adatoms of concentration $n_i = 15\%$, while their SOC is switched on (solid lines) or off (dotted lines). All curves are obtained by averaging $T_{pq}(E)$ over the energy interval $[-0.01\gamma_0, 0.01\gamma_0]$.

Figure S6 shows scaling of the transmission function $T_{pq} = {\rm Tr}[\mathbf{t}_{pq}\mathbf{t}_{pq}^\dagger]$ in Eq. (9) with the length L (at fixed width W) for electron paths from lead $2 \to 3$ and lead $2 \to 4$, as well as their difference, in six-terminal graphene device in Fig. 1 of the main text. The difference $T_{32} - T_{42}$ being positive means that more electrons arriving into lead 3 than in lead 4 will cause negative $R_{\rm NL}^{\rm qb}$ at some intermediate length scales. The slow decay of quantities in Fig. S6 characterizing the quasiballistic transport regime can manifest as long as the channel length L is smaller than the mean free path, which we estimate for $n_i = 15\%$ concentration of Au adatoms to be between 300 nm and 400 nm.

C. Six-terminal graphene geometry for isolating SHE contribution to $R_{\rm NL}$

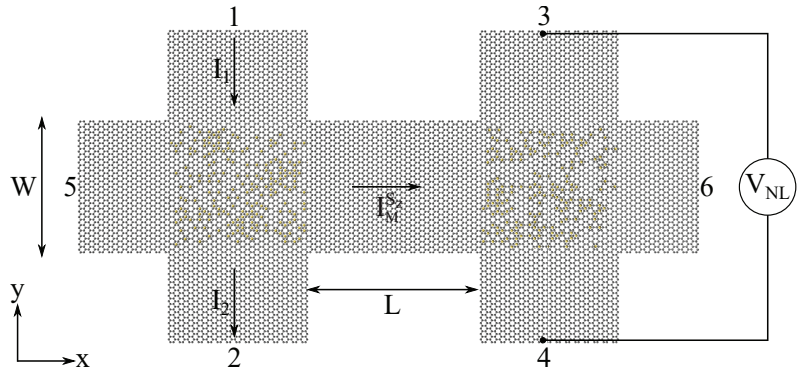

Fig. S7: Schematic view of our proposal for a six-terminal graphene geometry where adatoms are removed from the channel connecting the two crossbars in order to isolate $R_{\rm NL}^{\rm SHE}$.

Our interpretation of different contributions to $R_{\rm NL} = R_{\rm NL}^{\rm SHE} + R_{\rm NL}^{\rm Ohm} + R_{\rm NL}^{\rm qb} + R_{\rm NL}^{\rm pd}$ in Fig. 4 of the main text and their scaling with the length L of the device motivates us to propose a setup in Fig. S7 where adatoms are completely removed in the channel and $R_{\rm NL}^{\rm SHE}$ could be isolated and its maximum value quantified. When such ballistic channel is sufficiently long, $R_{\rm NL}^{\rm pd} = 0$ due to $L > W$ (see Fig. S5) and $R_{\rm NL}^{\rm qb}, R_{\rm NL}^{\rm Ohm} \to 0$ due to the absence of adatom-induced scattering in the channel. The mediative spin current $I_{\rm M}^{S_z}$ generated by the direct SHE in the left crossbar then arrives conserved at the right crossbar where it is converted into nonlocal voltage signal $V_{\rm NL}$ by the inverse SHE.

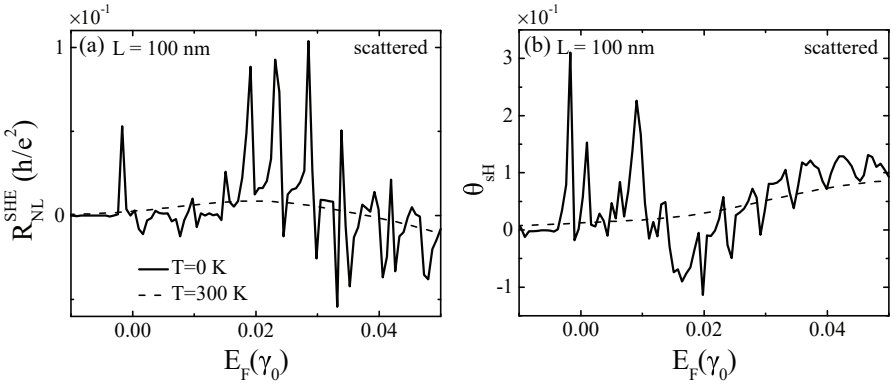

Fig. S8: (a) Nonlocal resistance $R_{\rm NL}^{\rm SHE}$ generated solely by the combination of direct SHE (in the left crossbar) and inverse SHE (in the right crossbar) in the setup of Fig. S7. (b) Spin Hall angle $\theta_{\rm sH}$ for the same setup in Fig. S7. The gold adatoms are distributed in scattered fashion with concentration $n_i = 15\%$ in each of the square regions within the two crossbars in Fig. S7.

The maximum value of $R_{\rm NL}^{\rm SHE}$ in Fig. S8 is still smaller than the absolute value of other contributions to $R_{\rm NL}$ in Fig. 4 of the main text at intermediate channel lengths L. We also find that both $R_{\rm NL}$ and $\theta_{\rm sH}$ exhibit sharp peak at about the same Fermi energy located very close to CNP, which demonstrates one-to-one correspondence between directly measurable charge transport quantity $R_{\rm NL}$ and indirectly inferred spin transport quantity $\theta_{\rm sH}$.

[1] M. Büttiker, Phys. Rev. Lett. **57**, 1761 (1986).
[2] C. W. Groth, M. Wimmer, A. R. Akhmerov, and X. Waintal, New J. Phys. **16**, 063065 (2014).
[3] A. Ferreira and E. R. Mucciolo, Phys. Rev. Lett. **115**, 106601 (2015).
[4] S. Roche, D. Mayou, Phys. Rev. Lett. **79**, 2518 (1997); S. Roche, Phys. Rev. B **59**, 2284 (1999).
[5] The spin conductivity in two-dimensions has the same unit as spin conductance and it is naturally given in the units of spin conductance quantum, $e/4\pi$ [19]. However, to make the spin Hall angle a dimensionless quantity, spin conductivity/conductance should be expressed in the same units as charge conductivity/conductance by replacing $e/4\pi$ with charge conductance quantum $e^2/h = (2e/\hbar)(e/4\pi)$.

[6] A. Dyrdal, V. K. Dugaev, and J. Barnas, Phys. Rev. B. **80**, 155444 (2009).
[7] C. L. Kane and E. J. Mele, Phys. Rev. Lett. **95**, 226801 (2005).
[8] L. Sheng, D. N. Sheng, C. S. Ting, and F. D. M. Haldane, Phys. Rev. Lett. **95**, 136602 (2005).
[9] A. Cresti, D. V. Tuan, D. Soriano, A. W. Cummings, and S. Roche, Phys. Rev. Lett. **113**, 246603 (2014).
[10] C. Weeks, J. Hu, J. Alicea, M. Franz, and R. Wu, Phys. Rev. X **1**, 021001 (2011).
[11] J. Balakrishnan *et al.*, Nat. Commun. **5**, 4748 (2014).
[12] A. Ferreira, T. G. Rappoport, M. A. Cazalilla, and A. H. Castro Neto, Phys. Rev. Lett. **112**, 066601 (2014).
[13] M. Milletari and A. Ferreira, arXiv:1601.08076; *ibid*, arXiv:1604.03111.
[14] A. Ferreira, *private communication.*
[15] J. H. Garcia and T. G. Rappoport, 2D Mater. **3**, 024007 (2016).
[16] B. K. Nikolić, L. P. Zârbo, and S. Souma, Phys. Rev. B **73**, 075303 (2006).
[17] C.-L. Chen, C.-R. Chang, and B. K. Nikolić, Phys. Rev. B **85**, 155414 (2012).
[18] K. Kazymyrenko and X. Waintal, Phys. Rev. B **77**, 115119 (2008); M. Wimmer and K. Richter, J. Comp. Phys. **228**, 8548 (2009).
[19] B. K. Nikolić, L. P. Zârbo, and S. Souma, Phys. Rev. B **72**, 075361 (2005).
[20] L. Sheng, D. N. Sheng, and C. S. Ting, Phys. Rev. Lett. **94**, 016602 (2005).
[21] J. Tworzydło, B. Trauzettel, M. Titov, A. Rycerz, and C. W. J. Beenakker, Phys. Rev. Lett. **96**, 246802 (2006).
[22] P.-H. Chang, F. Mahfouzi, N. Nagaosa, and B. K. Nikolić, Phys. Rev. B **89**, 195418 (2014).
[23] M. Titov, EPL **79**, 17004 (2007).